Experiments in Fluids 35 (2003) 178–187
DOI 10.1007/s00348-003-0645-6

Microbubble lensing-induced photobleaching (μ-BLIP) with application to microflow visualization

D. Sinton, D. Erickson, D. Li

Abstract The curvature of gas–liquid interfaces and the step change in properties across these interfaces in microchannels are shown here to create a powerful lens/mirror effect. In a hydrophilic system, light incident on the bubble is focused into the surrounding liquid, resulting in a locally increased total light exposure. The optical phenomena leading to this are discussed, and the effect is demonstrated experimentally by imaging the increased photobleaching rate of fluorophores in the near-bubble region. Numerical simulations of the system are performed to investigate the electrical potential and flow fields resulting from the application of an axial electric field. Microbubble lensing-induced photobleaching (μ-BLIP) is then applied as a method to inject a negative scalar flow marker for flow visualization in microchannels. Once formed, the electrokinetic transport of this marker is analyzed to determine the cross-channel velocity profile of the liquid phase and the liquid velocity in the film. Experimental data is verified by comparison with numerical predictions and previous experimental studies. This contribution represents both a new application of microscale gas–liquid interfacial phenomena, and a new technique for microfluidic flow visualization, particularly applicable (though not limited) to the study of multiphase microchannel flows.

1 Introduction

Microsized chemical synthesis and analysis systems can offer many advantages over their traditional, macrosized counterparts. Typical advantages include reduced reagent/sample use, increased sensitivity, increased speed of analysis, and potential for mass-manufactured, portable, disposable systems. The desire to miniaturize conventional multiphase systems has fostered recent interest in phase change and multiphase transport phenomena in microchannels (Chang 2002; Takhistov et al. 2002; Zhao et al. 2001). Potential applications include microsized evaporators, condensers, distillation units, gas–liquid reactors, multiphase extraction and separation units, and heat exchangers. Latent heat effects, central to the performance of many conventional heat exchangers, could be particularly useful in the thermal control of temperature-sensitive microfluidic chip applications. Bubbles may also be used in microfluidic chips to separate discrete liquid samples (Zhao et al. 2001), or employed as pumping mechanisms (Jun and Kim 1998). Knowledge of multiphase phenomena in microsystems is also required to avoid unwanted boiling of electrolyte in microchannels due to a lack of dissipation of Joule heating. This will be of increasing importance as microfluidic chip technologies mature into mass-produced polymer-based chips (Duffy et al. 1998; Ross et al. 2001), which are less efficient at dissipating heat than conventional glass chips, due to their low thermal conductivity.

A theoretical analysis of pressure-driven motion of a semi-infinite bubble in a circular capillary was presented by Bretherton (1961). Those results have since been extended to include discrete bubbles (Ratulowski and Chang 1989), the effect of surfactants (Ratulowski and Chang 1990), and other aspects. The effect of surfactant on the pressure required to advance a semi-infinite bubble is of particular relevance to pulmonary airway reopening conditions (Ghadiali and Gaver 2000). In microfluidic chip applications, however, pressure-driven multiphase transport is often not practical, as it can require orders of magnitude higher pressure gradients than single-phase liquid transport (Chang 2002). For this reason, electrokinetic bubble transport, described in detail by Takhistov et al. (2002), is an attractive option.

To study liquid flow in microchannels, various microflow visualization methods have evolved. Microparticle image velocimetry (microPIV) is a method that was adapted from well-developed PIV techniques for flows in macrosized systems (Taylor and Yeung 1993; Santiago et al. 1998; Meinhart et al. 1999). In that technique, the fluid motion is inferred from the motion of submicron tracer particles. To eliminate the effect of Brownian motion, temporal or spatial averaging must be employed. Particle affinities for other particles, channel walls, and free surfaces must also be considered. In electrokinetic flows, the

Received: 21 January 2003 / Accepted: 24 April 2003
Published online: 27 June 2003

D. Sinton, D. Erickson, D. Li (✉)
Department of Mechanical and Industrial Engineering,
University of Toronto, 5 King's College Road,
Toronto, Ontario, M5S 3G8, Canada
E-mail: dli@mie.utoronto.ca
Fax: +1-416-9787753

Financial support of this work by the Natural Sciences and Engineering Research Council (NSERC) of Canada, through post-graduate scholarships to D.S. and D.E. and a research grant to D.L., is gratefully acknowledged. Financial support from Glynn Williams, through a post-graduate scholarship to D.S. is also gratefully acknowledged.

electrophoretic motion of the particles (relative to the bulk flow) is an additional consideration. Dye-based microflow visualization methods have also evolved from their macrosized counterparts. However, traditional mechanical dye injection techniques are difficult to apply on the microscale. Specialized caged fluorescent dyes have been employed to facilitate this injection using selective light exposure. The photoinjection is accomplished by exposing an initially nonfluorescent solution seeded with caged fluorescent dye to ultraviolet light. As a result of the ultraviolet exposure, caging groups are broken and fluorescent dye is released. Lempert et al. (1995) first employed caged fluorescent dyes for flow tagging velocimetry in macrosized flows. This technique has since been used to study a variety of liquid flow phenomena in microstructures (Paul et al. 1998; Herr et al. 2000; Johnson et al. 2001; Molho et al. 2001; Sinton et al. 2002a, 2002b). The disadvantages of this technique are that it requires specialized caged dye (which is expensive), extensive infrastructure to facilitate the photo injection, and channel materials that transmit ultraviolet light. As an alternative to photoinjection of fluorescent dye, a flow marker can be created in a uniform solution of fluorescent dye by local photobleaching (Molho et al. 2001; Mosier et al. 2002). When a dye molecule is photobleached (or photodestroyed) it no longer fluoresces. Although the literature on this process is sparse, it is well established that the rate of photobleaching correlates directly with excitation light exposure (Becker 1996). None of these flow velocimetry methods have been applied to direct measurements of transport in multiphase microchannel applications. Instead, liquid velocities have been inferred from observed interface motion or by measuring reservoir levels by means of a capillary (Takhistov et al. 2002).

In this paper, the ability to intensify light exposure in the near-bubble liquid using the optical characteristics of the gas–liquid interface is demonstrated. The optical phenomena leading to this focusing are discussed, and the effect is shown experimentally by imaging the increased photobleaching rate of fluorophores in the near-bubble region. Numerical simulations are performed to investigate the electrical potential field and flow field in this system, resulting from the application of an axial electric field. Microbubble lensing-induced photobleaching is then applied as a method to inject a flow marker for flow visualization. The bubble film flow rates and the cross-channel velocity profiles determined are verified by comparison with numerical predictions and previous experimental studies. This contribution represents both a new application of microscale gas–liquid interfacial phenomena, and a new technique for microfluidic flow visualization, particularly applicable to (though not limited to) the study of multiphase microchannel flows.

2
Experiments

In the experiment, a length of capillary was filled with an aqueous fluorescein/buffer solution such that it contained a single bubble at the midpoint of the capillary. Each end of the capillary was connected to a reservoir, and the bubble region was viewed under an oil-immersion epi-illumination fluorescent microscope. The fluorescent emission of the liquid was imaged with a progressive scan CCD camera, digitized, and stored on the computer. Following the experiment, image processing was performed, and the images were analyzed. In cases where fluid flow was involved, scalar image velocimetry was performed to determine liquid velocities.

2.1
Imaging

Imaging was performed with a previously developed fluorescent microscope system (Sinton et al. 2002a, 2002b). A continuous uniform flood of excitation light was provided by a single-line 200-mW, 488-nm argon laser (American Laser Corp.), through the 25×, NA=0.75 oil immersion microscope objective (Leica). The index of refraction of the oil (n_{oil}=1.48) was matched to that of the capillary (n_{fused_silica}=1.46), to avoid lensing caused by the curvature of the capillary. The camera was run in video mode at 15 Hz with individual exposure times of 1/60 s. Because of the geometry of the CCD chip, the camera captured only a square central portion of the field of view illuminated by the microscope optics. The acquired images had a resolution of 640×484 pixels. This corresponded to a 543-μm visible length of capillary, with each pixel representing a 0.85-μm square in the object plane. The camera orientation was carefully adjusted such that the pixel grid was aligned with the radial and axial directions.

2.2
Image processing

To remove any nonuniformities present in the imaging system, dark-field image subtraction and bright-field image normalization were performed with each image (Russ 1999). The bright-field image was obtained by imaging the channel filled with a uniform concentration of fluorescent dye without a bubble present. The pixel intensity values were then scaled linearly by a single factor such that the degree of photobleaching that occurred spanned the grayscale range. Finally, the images were smoothed with a distance based 10×10 pixel kernel. Pixel intensities of postprocessed images were directly interpreted as dye concentration based on a previously determined linear camera response characteristic.

2.3
Microchannels

The microchannels were 100-μm i.d., 15-cm long, circular cross-section fused silica capillaries (Polymicro Tech.). At the capillary midpoint, the exterior polyimide coating was oxidized and removed to create a viewing window. New capillaries were prepared by flushing with pure water followed by buffer, and then buffer with fluorescent dye. To inject the bubble, air was drawn into the capillary by suction provided by a low-volume high-pressure syringe (10 μL, Hamilton Gastight). The air was then slowly pumped out until only the bubble length desired remained in the capillary. At that point, the capillary end was reinserted into the solution and the bubble was drawn to the capillary midpoint. Each end of the capillary was then

connected to a small reservoir with embedded platinum electrodes.

2.4 Chemicals

The fluorescent dye employed here was fluorescein, 332 MW (Molecular Probes). The dye was dissolved to a concentration of c_o=50 μM in sodium (bi)carbonate buffer at *pH*=9.0, *I*=0.050 M. Rhodamine B was also used in preliminary tests. Although microbubble lensing-induced photobleaching (μ-BLIP) was clearly observed with rhodamine B, its fluorescence intensity is strongly temperature dependant. To isolate photobleaching from thermal effects, fluorescein (which is relatively insensitive to temperature) was used. Immediately before use, all solutions were filtered using 0.2-μm pore size syringe filters.

3 Results and discussion

3.1 Microbubble lensing-induced photobleaching (μ-BLIP)

When light is incident on an interface, it refracts according to Snell's Law (Hecht 2001)

$$n_1 \sin\theta_1 = n_2 \sin\theta_2, \quad (1)$$

where n and θ are the index of refraction and transmission angle (relative to the local interface normal), respectively, and subscripts 1 and 2 denote the medium. Thus, when the light is traveling from a higher-index medium (n_1) to a lower-index medium (n_2), the light bends away from the normal. Light incident at the critical angle $\theta_1=\theta_c$ is refracted along the interface (θ_2=90°) where

$$\theta_c \ \sin^{-1}(n_1/n_2), \ n_1 > n_2 \quad (2)$$

Any light incident at an angle greater than the critical angle is totally reflected back into the higher-index medium. The effect of this phenomenon, termed total internal reflection (TIR), is illustrated in the backlit image shown in Fig. 1a. The edges of the air bubble are visible in the transparent aqueous solution because the index of refraction of air (n_{air}=1.0) is less than that of water (n_{water}=1.3). The edges of the bubble appear dark because the light (from below) is reflected in this region, where the angle of incidence relative to the local interface normal is greater than the critical angle of θ_c=50°. This darkening does not occur in the center of the bubble where the angle between the local interfacial normal and the incident light is less than the critical angle (i.e. the interface is more perpendicular to the incident light). The same phenomena, though to a lesser extent, darkens the channel–liquid interface where $n_{channel}$=1.46<n_{water}. This darkening makes the channel walls visible in Fig. 1a, and is one of the key factors that limit near-wall resolution of microflow visualization methods (Sinton et al. 2002b). When the liquid is seeded with fluorescent dye and excitation light is applied, the bubble interface will also reflect the green fluorescent emission from the liquid. The 'bright-spot' optical artifacts shown in Fig. 1b evidence the reflection of fluorescent light generated in the liquid off the bubble caps. Note that this is not the blue (λ=488 nm) excitation light because, through filtering, only green fluorescent emission (λ>510 nm) is passed to the camera. In a similar manner, the blue excitation light from the microscope is reflected at the bubble interface as illustrated in Fig. 2. Figure 2a illustrates that uniform excitation light exposure in a liquid-only capillary would cause a spatially uniform rate of fluorescence, and in turn, a spatially uniform rate of photobleaching. The addition of an air bubble alters the

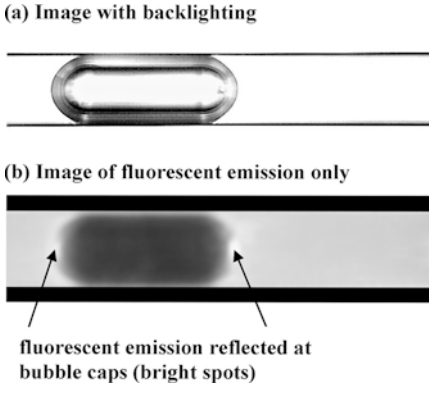

Fig. 1a,b. Images of a bubble: **a** With backlighting. **b** With fluorescent emission from the liquid phase

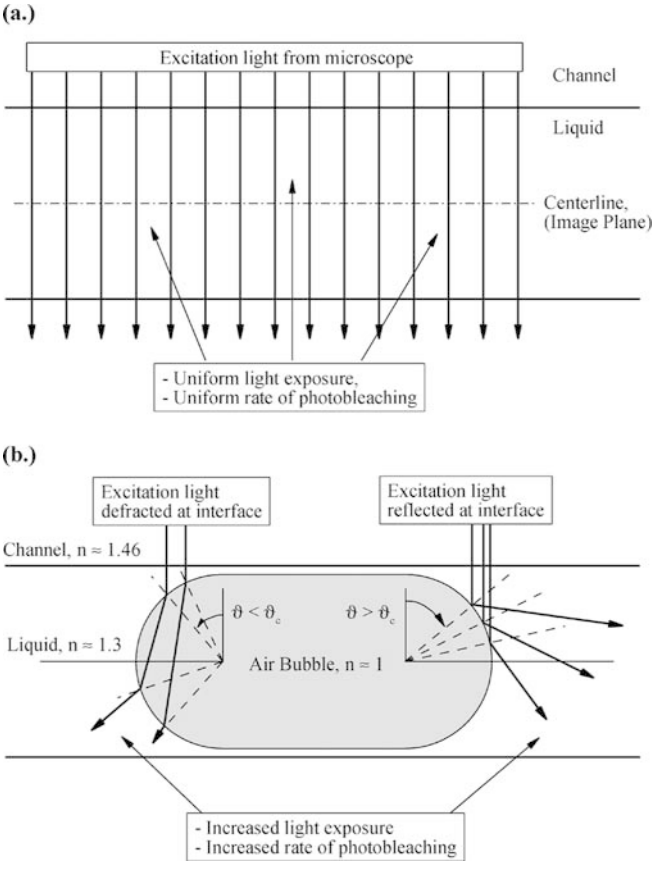

Fig. 2a,b. Illustrative schematics of optical phenomena: **a** Uniform photobleaching in a liquid-filled channel. **b** Increased photobleaching in the near-bubble liquid because of the presence of a bubble

path of the excitation light depending on its angle of incidence with respect to the local interface normal. Thus, excitation light may be refracted or reflected at the interface as illustrated in Fig. 2b. Light incident at angles greater than the critical angle is reflected back into the liquid as shown on the right in Fig. 2b. Light incident at angles less than the critical angle is refracted at both interfaces and transmitted back into the liquid as shown on the left in Fig. 2b. In both ways the intensity of the excitation light is increased in the liquid near the bubble. This results in higher total excitation light exposure, initially higher fluorescence intensity, and a higher rate of photobleaching, which in time results in lower fluorescence intensity. This local photodestruction is the result of microbubble lensing-induced photobleaching (μ-BLIP).

It is important to note that Fig. 2 and the above explanation are simplifications of the real case. The two-dimensional model of the bubble cap is reasonable considering the hemispherical geometry of the interface. However, the excitation light beam is, in reality, conical, due to the high numerical aperture objective used. This adds a layer of complexity to the optical analysis, but the physics remains the same as that illustrated in Fig. 2. In addition, lensing and increased photobleaching in the liquid film between the bubble and the wall (similar to waveguide or fiber-optic light transmission) is also expected. Because of the small thickness of the film, however, the volume of liquid photobleached in this region does not contribute significantly compared to that photobleached at the bubble caps. For the same reason, the extent of photobleaching is essentially independent of bubble length.

The image sequence in Fig. 3 demonstrates the μ-BLIP process. Figure 3a is an image of the uniform fluorescent emission of the dye-filled channel without a bubble. The image in Fig. 3b was taken shortly after the bubble was moved into position. Although both caps contribute equally to the photobleaching, the camera's field of view is focused on the right cap, the point of which has a 'bright-spot' reflection as discussed previously. In Fig. 3b the fluorescent emission appears fairly uniform throughout the liquid at the level of the original dye concentration without a bubble (Fig. 3a). The images in Fig. 3b–f were taken in sequence at 20/15-s (1.33-s) intervals, and processed identically. Significant darkening in the near-bubble liquid is apparent. The radial orientation of the dark/bright ray pattern (believed to be caused by interference) is further evidence of the bubble lensing phenomena. After 5.3 s (Fig. 3f), a significant photobleached region is formed around the bubble, where as the dye at the right-hand side of the camera view has retained the original intensity level. This is more apparent in the axial concentration profiles shown in Fig. 4, where the five profiles correspond to the image sequence in Fig. 3b–f. As shown in Fig. 4, the bulk of the photobleaching occurs during the first 2 s. The broadening of the dark region beyond that is mostly due to diffusion of the photobleached dye. Increasing the excitation light energy and correspondingly decreasing the exposure time could reduce this axial broadening. Allowing time for radial diffusion, however, creates a more uniform, axially symmetric photobleached

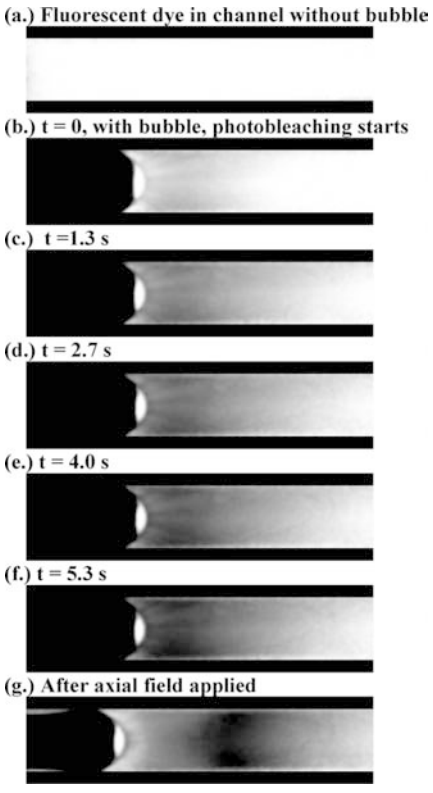

Fig. 3. **a** Image of fluorescent emission from a liquid-filled capillary. **b–f** Image sequence demonstrating the μ-BLIP process. **g** Image of photobleached dye advected with electro-osmotic flow

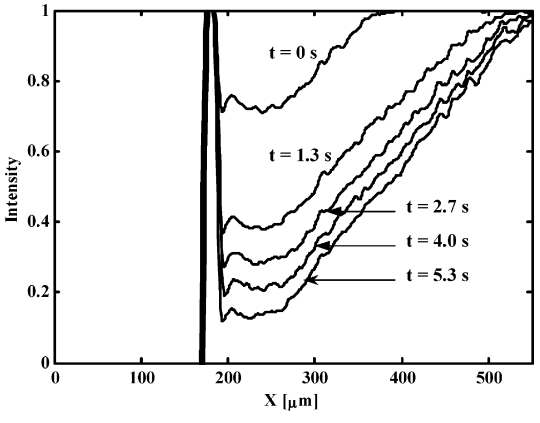

Fig. 4. Axial fluorescence intensity profiles corresponding to the image sequence in Fig. 3b–f. The bulk of the photobleaching occurs close to the interface and in the first few seconds of exposure

region. For the most part, experimental parameters such as these (solutions, light intensities, exposure durations) were chosen out of convenience, and it is likely that performance could be improved with optimization. One option is to use high molecular weight dyes such as fluorescein-dextran conjugates (Molecular Probes), which are less susceptible to diffusion than standard dyes.

The image in Fig. 3g was taken after an axial electric field was applied to the channel. The resulting electro-osmotic liquid flow transformed the dye photobleached at both bubble caps into a dark cross-stream liquid flow

marker. The electrokinetic transport of the bulk liquid in this system is calculated numerically. These simulation results, particularly the shape of the electric field, establish that it is reasonable to assume that the electrophoretic velocity of the marker is purely axial at distances greater than 1 diameter from the bubble cap. Scalar image velocimetry is then applied to a μ-BLIP-generated flow marker for experimental determination of the cross-stream liquid velocity profile in the microchannel. Accurate cross-stream velocity measurements were obtained with this technique purely by experimental means.

3.2 Numerical analysis

In order to develop the underlying physics of the μ-BLIP process, a series of numerical simulations were conducted using the BLOCS (Bio-lab-on-a-chip simulation) finite element code (Sinton et al. 2002a; Erickson and Li 2002a; Erickson and Li 2002b). Here we provide some brief details on the numerical method, concentrating on the implementation of the code to this application. For further details, including comments on general verification of the code and computational expense, the reader is referred to Erickson and Li (2002a). In these simulations we considered a long axially symmetric capillary, with a diameter equivalent to those used in the aforementioned experiments (100 μm), with a 200-μm long stationary bubble located at the midpoint. The liquid domain geometry was then discretized using nine-noded biquadratic elements, which were significantly refined in the region near the bubble and coarsened near the capillary entrance and exit.

The first stage of the numerical analysis is the determination of the applied potential field in the liquid system, which, for the case of a constant conductivity electrolyte, can be determined from the Laplace equation

$$\nabla^2 \phi = 0, \tag{3}$$

where ϕ is the applied potential field. Requiring that the solution remain finite at the capillary axis and applying insulation conditions, $\partial\phi/\partial n$ where n is the normal to the surface, were used along the bubble and capillary walls. The electric field lines generated for the case equivalent to 2600 V applied over the 15-cm capillary (consistent with the experiments discussed in Sect. 3.3) are shown in Fig. 5a. Since the liquid cross-sectional area is significantly reduced, and thus the local channel resistance is greatly increased, the electric field lines are concentrated in the thin film that surrounds the bubble. This has the effect of increasing the gradient of ϕ within this region and reducing it far away from the bubble. This is demonstrated in Fig. 5b, which shows the change in ϕ along the length of the capillary for the no-bubble case, a bubble with a 0.5-μm film thickness, and a bubble with a 0.1-μm film thickness. The presence of the bubble reduces $\partial\phi/\partial x$ to 86% and 96% of that for the no-bubble case for the 0.1-μm film thickness and 0.5-μm film thickness, respectively. Also of interest in Fig. 5a is the shape of the isopotential

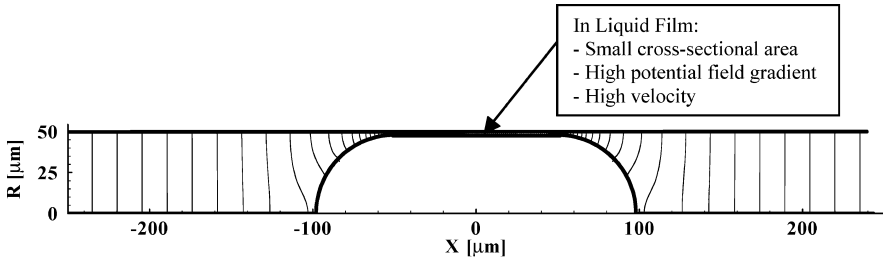

(a.)

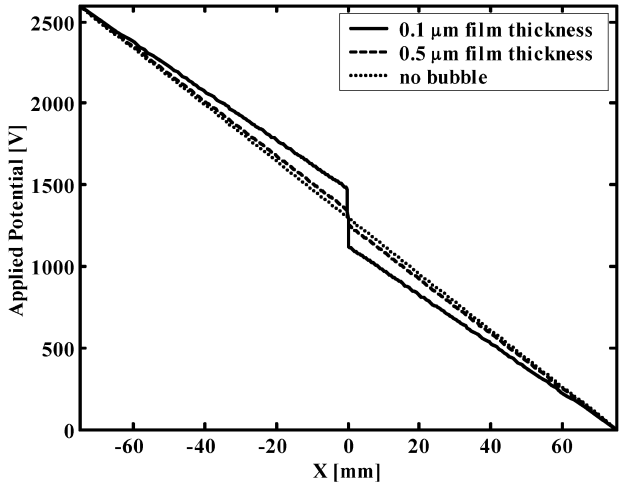

(b.)

Fig. 5. **a** Numerically determined isopotential lines in the presence of an insulating bubble. **b** Influence of bubble film thickness on the global applied electric field

lines, which assume a slightly curved shape beyond the thin film on either side of the bubble. At a distance less that one capillary diameter from the edge of the bubble, however, they are nearly perpendicular to the channel wall. This limited influence of the bubble on the shape of the isopotential field lines facilitates the use of μ-BLIP as a microflow visualization technique.

With the potential field solution developed, the flow field can be determined using the low-Reynolds-number Stokes equations, Eq. 4a and the compressibility condition Eq. 4b

$$0 = -\nabla p + \mu \nabla^2 u, \tag{4a}$$

$$\nabla \cdot u = 0, \tag{4b}$$

where u is the fluid velocity, p is the pressure and μ is the viscosity. In principal, Eq. (4a) should contain an electrical body force term resulting from the application of the electric field to the net charge density in the double layer. In this analysis, however, we assume an electro-osmotic slip velocity $u_{eo}=v_{eo}E$, where v_{eo} is the electro-osmotic mobility (taken as $6.2\text{x}10^{-8}$ m^2/Vs (Duffy et al. 1998)) and E is the gradient of ϕ tangential to the surface, applied along the capillary wall. This simplification eliminates the double-layer formulation and has proven accurate in transport cases, such as that examined here, where the double-layer thickness is very thin compared with the capillary diameter (Sinton et al. 2002a; Erickson and Li 2002a). In this case the condition is slightly more stringent as the double-layer thickness must be thinner than the film surrounding the bubble. In the case examined the ionic strength of the buffers is on the order of 10^{-2} M, which gives us a double-layer thickness on the order of 3 nm. As shown in the proceeding section, this is several orders of magnitude smaller than the film thickness encountered here. Applying this slip boundary condition along the capillary wall, a bounded condition along the capillary axis, and a zero tangential shear condition along the bubble (Erickson et al. 2002c) yields the near-bubble flow field shown in Fig. 6a. The velocity profiles at 0.1, 0.4 and 1.0 capillary diameters away from the edge of the bubble are shown in more detail in Fig. 6b. As can be seen, very near the bubble the velocity close to the capillary wall is slightly higher than that at the center; however, it very rapidly evolves to the traditional plug-type velocity profile expected for electro-osmotic flow. This result is used as a verification of the microflow visualization technique developed in the following section.

3.3 Microflow visualization with a μ-BLIP-generated flow marker

Methods for inferring a bulk fluid velocity by analyzing a sequence of images of dye transport fall under the broad category of scalar image velocimetry (Dahm et al. 1992; Tokumaru and Dimotakis 1995). In general, the goal of these methods is to extract the bulk fluid velocity vector

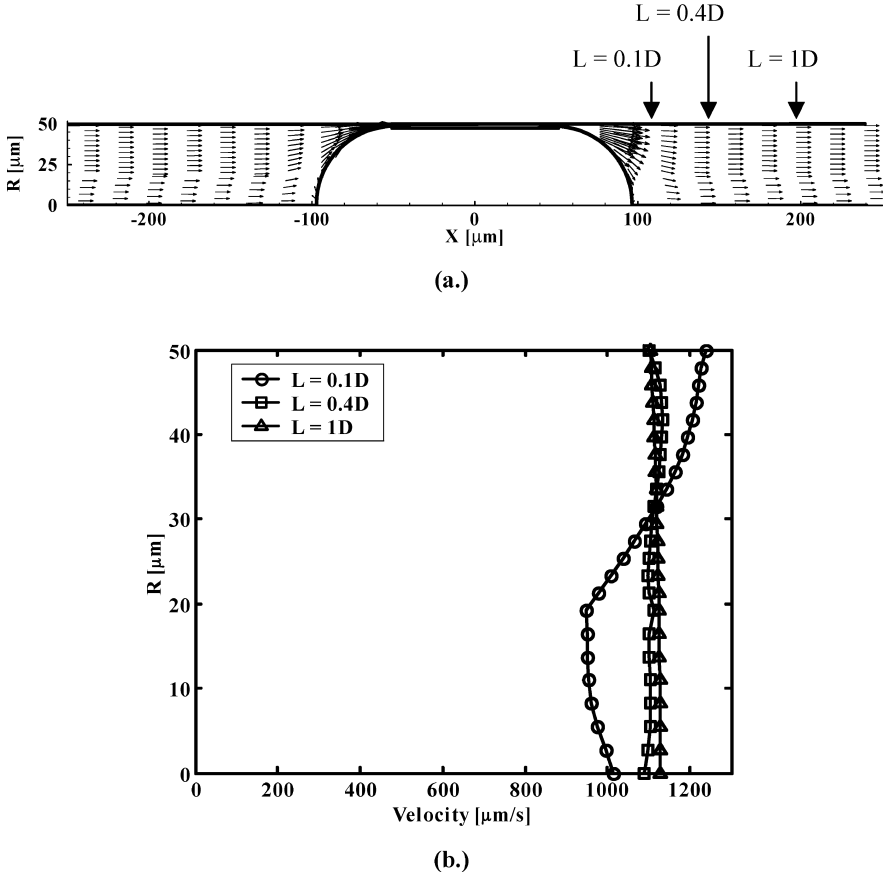

Fig. 6. **a** Numerically determined electro-osmotic flow field in the near bubble region. **b** *X*-direction velocity profiles at various distances from the bubble edge. *L* denotes distance from the edge of the bubble

u from the advective terms of the mass conservation equation satisfied by the imaged dye species

$$\frac{\partial c}{\partial t} + u \cdot (\nabla c) = D\nabla^2 c, \tag{5}$$

where c is the concentration of dye species, and D is the diffusion coefficient. The analysis may be greatly simplified when applied to internal, fully-developed flows by using a discrete dye sample. This is because the motion of the locus of dye concentration maxima is, for the most part, not affected by diffusion and reflects the bulk motion of the fluid. This maximum concentration tracking method has been applied in caged-dye-based microfluidic flow visualization studies (Herr et al. 2000; Sinton et al. 2002b). In those cases, a photoinjection of fluorescent dye provided the only nonzero dye concentration c in an otherwise nonfluorescent solution. In the case of μ-BLIP, however, the solution contains a uniform dye concentration, $c=c_0$, and a portion of the dye is photochemically destroyed. Since the fluorescent dye concentration c is a conserved quantity, the concentration of photodestroyed dye c^* is also conserved. Thus Eq. (5) is satisfied for $c=c^*$, where

$$c* = (c_0 - c). \tag{6}$$

Thus 'maximum' concentration tracking methods can be directly applied to inverted and linearly scaled intensity images of a photobleached sample. Equivalently one may think of the conserved quantity as the photodestroyed fluorophores whose concentration is quantified by a lack of fluorescence.

Once the near-bubble liquid was photobleached (as shown in Fig. 3), an axial electric field was applied by setting the upstream (left) reservoir potential to 2600 V, and connecting the downstream (right) reservoir to ground. The camera recorded the resulting transport of the photobleached sample. A five-image sequence taken at 1/15 s intervals is given in Fig. 7a. The electro-osmotic liquid flow has combined the dye photobleached at both bubble caps into a dark, cross-stream, band, which is advected downstream with the electro-osmotic flow. The bubble itself is shown to have a finite velocity in the direction opposite to the electro-osmotic liquid flow.

The concentration field of photobleached dye c^* was calculated for each image using image-processing software developed in-house. Axial marker concentration profiles of the images shown in Fig. 7a are given in Fig. 7b. The vertical lines on the left in Fig. 7b indicate the motion of the interface, and the profiles on the right show the marker transport. A relatively clear concentration maximum is apparent in each profile. To determine the bubble velocity the distance between the vertical lines may be divided by the corresponding time step. Here a bubble velocity of $u_{\text{bubble}}=-190$ μm/s was determined. To determine the velocity profile in the liquid region, the point of maximum concentration was located along each axial line of pixels, using a weighted average of the highest concentration values in the liquid phase. The set of maximum concentration points from each image

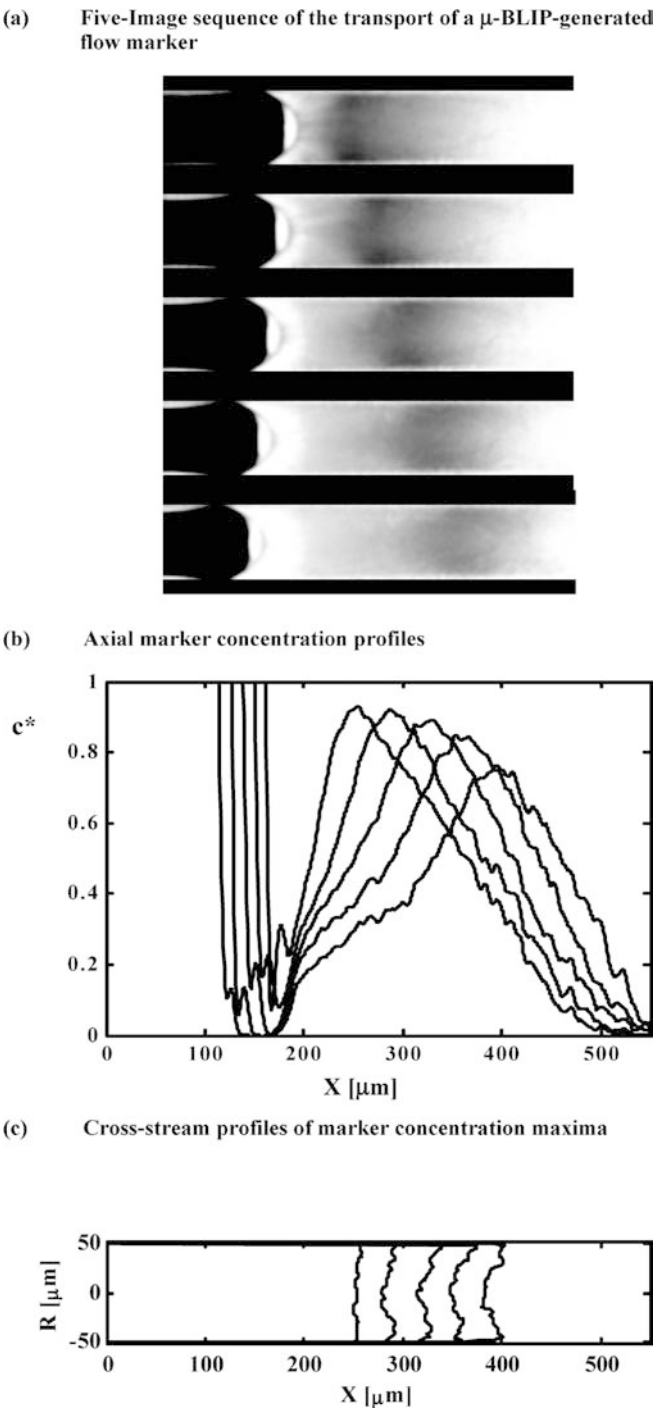

Fig. 7. **a** An image sequence of the μ-BLIP-generated flow marker in the electro-osmotic flow. **b** Corresponding axial concentration profiles of the flow marker. **c** Corresponding cross-stream profiles of marker concentration maxima

formed the cross-stream concentration maxima profiles shown in Fig. 7c. In a given sequence, any pair of concentration profiles could provide a velocity distribution by dividing the distance between them by the corresponding time-step. Here, all five profiles were used in an error-weighted average to determine the velocity data. Once calculated, this velocity data represents the 'observed' velocity of the marker u_{ob}. Since the dye molecules are charged, the observed velocity of the

concentration maxima is the summation of the bulk fluid velocity u_{eo} and the electrophoretic velocity of the dye u_{ph} as follows:

$$u_{ob} = u_{eo} + u_{ph}. \quad (7)$$

The electrophoretic velocity u_{ph} must be calculated directly from the electrophoretic mobility v_{ph} and the applied electrical field strength E as

$$u_{ph} = v_{ph}E. \quad (8)$$

The electrophoretic mobility of fluorescein may be taken as $v_{ph}=-3.3\times10^{-8}$ m^2/Vs (Paul et al. 1998; Sinton et al. 2002b). The local axial applied electric field, however, requires special consideration here. Through the numerical simulations it was shown that the isopotential lines became almost totally radial less than one diameter away from each bubble cap (Fig. 5a). Thus it is reasonable to assume that the electrophoretic velocity of the marker is purely axial (aligned with the potential gradient vector $\vec{E}$). In the case of a channel containing no bubble and filled with a uniform electrolyte solution, the magnitude of the axial electric field may be calculated simply by dividing the applied voltage differential ΔV by the length of the channel L. As shown in the numerically determined axial potential profiles in Fig. 5b, the bubble adds resistance to the channel and hence causes a field reduction in the liquid far away from the bubble. To experimentally determine this reduced field strength in the liquid, the current was measured both with and without the bubble present, and the following calculation performed:

$$E_B = E_{NB}\left[\frac{i_B}{i_{NB}}\right], \quad (9)$$

where i is the electrical current draw, subscript B indicates the presence of a bubble, and subscript NB indicates that no bubble is present. The bracketed current ratio in Eq. (9) is the factor by which the electric field is reduced from the overall value ($\Delta V/L$) due to the presence of the bubble. A plot of the currents measured with and without the bubble present versus the overall applied electrical field strength is given in Fig. 8. Both curves trend slightly upwards because of Joule heating-induced increases in fluid temperature (Swinney and Bornhop 2002; Sinton and Li 2003). The current ratio (in Eq. (9)), however, was found to be relatively constant at 0.85±0.025 over this range of applied field. Thus according to these current measurements and Eq. (9), the applied voltage drop of ΔV=2600 V over the L=0.15-m length of capillary generated an electrical field strength of E=14.7 kV/m in the liquid region. This is consistent with the decrease in E observed for the 0.1-μm film thickness case shown in Fig. 5b, suggesting the film thickness is of this order. Using this E value to calculate the electrophoretic marker velocity in Eq. (8), and substituting the result into Eq. (7), gave the bulk liquid electro-osmotic velocity profile shown in Fig. 9. The flat plug-like profile observed is characteristic of electro-osmotic flows and is in keeping with the corresponding numerically predicted velocity profile in Fig. 6. From the wall velocity, the electro-osmotic mobility

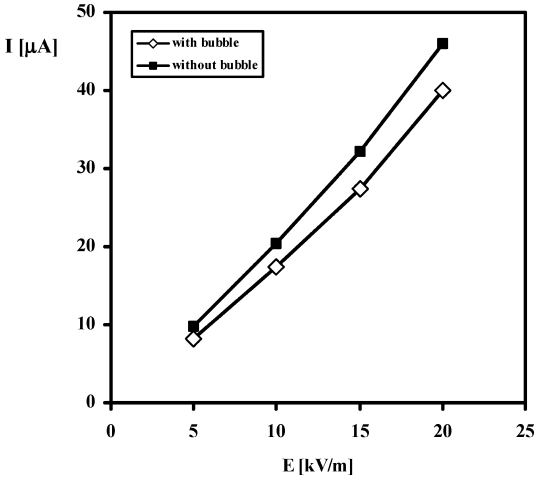

Fig. 8. A plot of the current values measured versus the overall electrical fields applied to the channel with and without a bubble present

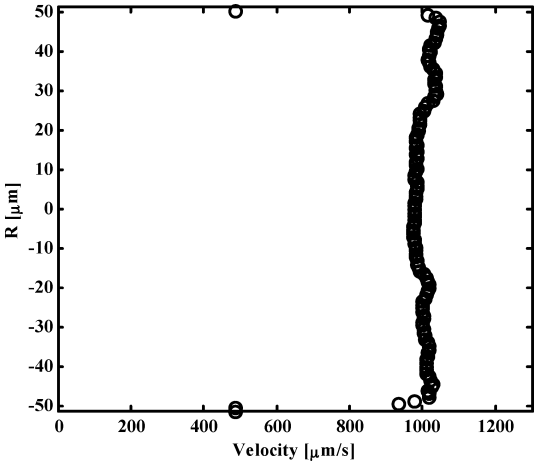

Fig. 9. Cross-stream electro-osmotic liquid velocity profile obtained by applying scalar image velocimetry to the transport of the μ-BLIP-generated flow marker

was calculated to be $v_{eo}=6.8\times10^{-8}$ m^2/Vs, in reasonable agreement with the value of $v_{eo}=6.2\times10^{-8}$ m^2/Vs reported by Duffy et al. (1998). The plug-like velocity profile achieved with the μ-BLIP-generated flow marker extends to within 4 μm from each wall. This degree of near-wall resolution is comparable to, and in many cases improved over, that achieved with caged-dye based microflow visualization techniques that involve increased infrastructure and specialized chemicals. In the general context of microflow visualization techniques, a clear disadvantage of μ-BLIP is the requirement that a bubble be present to facilitate the photoinjection of the flow marker. It was demonstrated here, however, that measurements of the cross-stream velocity profile in the microchannel can be obtained, free from bubble-induced two-dimensional electrical and hydrodynamic effects. Thus, this technique is a candidate for studying a variety of other aspects of electrokinetic channel flow for which caged-dye imaging has been employed such as the effects of joule heating, band spreading in corners, and pressure disturbances. An

advantage of this technique is the ability to concurrently image the bubble geometry, bubble velocity, and the local fluid velocity in multiphase systems. In this case, the effective film thickness was both measured (through current measurements) and calculated (through numerical simulations shown in Fig. 5) to be less than 1 μm. Near the bubble caps, the interface is optically indistinguishable from the wall, indicating that the film in that area is less than 1 μm. However, the images in Fig. 7a also show significant film thickening in the middle region of the bubble. This film thickening is a result of elongation of the bubble, which occurs upon application of the applied electric field. We expect that this elongation and the motion of the bubble are caused by the presence of mobile ionic surface charges inducing a differential net charge on the bubble caps, potentially in combination with changes in surface tension because of the presence of the high electric field strength in the film (electrocapillary effects). Film thickening results in lower liquid velocities in that portion of the film. By integrating the cross-stream velocity profile (Fig. 9), and determining the bubble velocity from the interface movement in Fig. 7b, the liquid film velocity was determined to be 3.3 mm/s at the bubble midpoint and an estimated 30 mm/s near the bubble caps. This demonstrates the applicability of this technique to the study of coupled dynamic transport phenomena, characteristic of microscale multiphase systems.

4 Conclusions

In this work, a method to intensify light exposure in the near-bubble liquid using the optical characteristics of the gas–liquid interface is proposed and demonstrated experimentally. The method takes advantage of the curvature and the step change in properties across a gas–liquid interface to create a lens/mirror optical arrangement in which light incident on the bubble is focused into the surrounding liquid, resulting in a locally increased total light exposure. The effect is demonstrated experimentally by imaging the increased photobleaching rate of fluorophores in the near-bubble region.

Based on these phenomena, a microbubble lensing-induced photobleaching (μ-BLIP) technique is then developed and applied as a method to inject a marker for flow visualization. A series of numerical simulations on the multiphase system demonstrated that both the isopotential lines and the flow field are disturbed by the presence of the bubble, however, the effect is limited to the near-bubble region (typically less than 1 capillary diameter from the edge of the bubble). Using the μ-BLIP technique, the electrokinetic transport of the photobleached marker is analyzed to determine the cross-channel velocity profile of the liquid phase and the liquid velocity in the film. These results are in good agreement with the numerical predictions and are consistent with velocity measurements from previous studies. The numerical simulations establish that it is reasonable to assume that the electrophoretic velocity of the marker is purely axial (aligned with the potential gradient vector $\bar{E}$) at distances greater than 1 diameter from the bubble cap. As demonstrated, accurate cross-stream velocity measurements were obtained with this technique purely by experimental means. This contribution represents both a new application of microscale gas–liquid interfacial phenomena and a new technique for microfluidic flow visualization, particularly applicable to (though not limited to) the study of multiphase microchannel flows.

References

Becker PL (1996) Quantitative fluorescence measurements. In: Wang XE, Herman B (ed) Fluorescence imaging spectroscopy and microscopy. Wiley, New York

Brethreton FP (1961) The motion of long bubbles in tubes. J Fluid Mech 10:166–188

Chang HC (2002) Bubble/drop transport in microchannels. In: Gad-el-Hak M (ed) The MEMs handbook. CRC, Boca Raton

Dahm WJA, Su LK, Southerland KB (1992) A scalar imaging velocimetry technique for fully resolved four-dimensional vector velocity fluid measurements in turbulent flows. Phys Fluids A 4:2191–2206

Duffy DC, McDonald JC, Schueller OJA, Whitesides GM (1998) Rapid prototyping of microfluidic systems in poly(dimethylsiloxane). Anal Chem 70:4974–4984

Erickson D, Li D (2002a) Influence of surface heterogeneity on electrokinetically driven microfluidic mixing. Langmuir 18:1883–1892

Erickson D, Li D (2002b) Microchannel flow with patch-wise and periodic surface heterogeneity. Langmuir 18:8949–8959

Erickson D, Li D, Park C (2002c) Numerical simulations of capillary driven flows in nonuniform cross sectional capillaries. J Colloid Interface Sci 250:422–430

Ghadiali SN, Gaver DP (2000) An investigation of pulmonary surfactant physicochemical behavior under airway reopening conditions. J Appl Physiol 88:493–506

Hecht E (2001) Optics, 4th edn. Addison-Wesley, New York

Herr AE, Molho JI, Santiago JG, Mungal MG, Kenny TW, Garguilo MG (2000) Electro-osmotic capillary flow with nonuniform zeta potential. Anal Chem 72:1053–1057

Johnson TJ, Ross D, Gaitan M, Locascio LE (2001) Laser modification of preformed polymer microchannels: application to reduce band broadening around turns subject to electrokinetic flow. Anal Chem 73:3656–3661

Jun TK, Kim CJ (1998) Valveless pumping using traversing vapor bubbles in microchannels. J Appl Phys 83:5658–5664

Lempert WR, Magee K, Ronney P, Gee KR, Haugland RP (1995) Flow tagging velocimetry in incompressible flow using photoactivated nonintrusive tracking of molecular motion (PHANTOMM). Exp Fluids 18:249–257

Meinhart CD, Wereley ST, Santiago JG (1999) PIV measurements of a microchannel flow. Exp Fluids 27:414–419

Molho JI, Herr AE, Mosier BP, Santiago JG, Kenny TW (2001) Optimization of turn geometries for microchip electrophoresis. Anal Chem 73:1350–1360

Mosier BP, Molho JI, Santiago JG (2002) Photobleached-fluorescence imaging for microflows. Exp Fluids 33:545–554

Paul PH, Garguilo MG, Rakestraw DJ (1998) Imaging of pressure- and electrokinetically driven flows through open capillaries. Anal Chem 70:2459–2467

Ratulowski J, Chang HC (1989) Transport of gas bubbles in capillaries. Phys Fluids A 1:1642–1655

Ratulowski J, Chang HC (1990) Marangoni effects of trace impurities on the motion of long gas bubbles in capillaries. J Fluid Mech 210:303–328

Ross D, Johnson TJ, Locascio LE (2001) Imaging of electro-osmotic flow in plastic microchannels. Anal Chem 73:2509–2515

Russ JC (1999) The image processing handbook, 3rd edn. CRC, Boca Raton

Santiago JG, Wereley ST, Meinhart CD, Beebe DJ, Adrian RJ (1998) A particle image velocimetry system for microfluidics. Exp Fluids 25:316–319

Sinton D, Erickson D, Li D (2002a) Photoinjection based sample design and electro-osmotic transport in microchannels. J Micromech Microeng 12:898–904

Sinton D, Escobedo-Canseco C, Ren L, Li D (2002b) Direct and indirect electro-osmotic flow velocity measurements in microchannels. J Colloid Interface Sci 254:184–189
Sinton D, Li D (2003) Electro-osmotic velocity profiles in microchannels. Colloids Surf A, in press
Swinney K, Bornhop DJ (2002) Quantification and evaluation of Joule heating in on-chip capillary electrophoresis. Electrophoresis 23:613–620
Takhistov P, Indeikina A, Chang HC (2002) Electrokinetic displacement of air bubbles in microchannels. Phys Fluids 14:1–14
Taylor JA, Yeung ES (1993) Imaging of hydrodynamic and electrokinetic flow profiles in capillaries. Anal Chem 65:2928–2932
Tokumaru PT, Dimotakis PE (1995) Image correlation velocimetry. Exp Fluids 19:1–15
Zhao B, Moore JS, Beebe DJ (2001) Surface-directed liquid flow inside microchannels. Science 291:1023–1026